

# Raman Spectroscopic Investigation of Friedel's Salt

Yanfei Yue<sup>ab</sup>, Jing Jing Wang<sup>c\*\*</sup>, P. A. Muhammed Basheer<sup>d</sup> and Yun Bai<sup>b\*</sup>

<sup>a</sup>College of Materials Science and Engineering, Chongqing University, 174 Shazheng Street, Shapingba, Chongqing, China 400044

<sup>b</sup>Department of Civil, Environmental and Geomatic Engineering, University College London, Gower Street, London, UK, WC1E 6BT

<sup>c</sup>CRANN and AMBER Research Centres, Trinity College Dublin, Dublin 2, Dublin, Ireland

<sup>d</sup>School of Civil Engineering, University of Leeds, Woodhouse Lane, Leeds, UK, LS2 9JT

## Abstract

Friedel's salt (FS) forms upon chloride binding in monosulphoaluminate (AFm) phase. This removes chlorides from the pore solution, hence, delays the initiation of steel-bar corrosion. Apparently, characterising and, in particular, monitoring the formation and the status of FS facilitate the prediction of the service life of reinforced concrete structures. Raman spectroscopy offers a potential for investigating FS. The current work characterised FS, including the synthesised pure FS, and the FS formed in a Portland cement (PC) paste powder, using a bench-mounted Raman spectrometer. The results revealed the full Raman spectra of pure FS between 200 ~ 4000  $\text{cm}^{-1}$ , including the featured Raman bands at 534/568  $\text{cm}^{-1}$  and 783  $\text{cm}^{-1}$  which correspond to the Al-OH stretching and bending vibration of FS respectively. Furthermore, similar Raman bands of FS were identified in PC paste sample subjected to accelerated chloride attack, further confirming the potential of Raman spectroscopy for distinguishing FS in cementitious materials.

**Keywords:** Cementitious materials, Chloride attack, Friedel's salt, Raman spectroscopy.

## 1. Introduction

Chlorides affect both the properties of concrete and steel embedded in it significantly. They can be introduced into concrete either internally or externally [1-4]. For the intermixed chlorides (usually from the mixing-water), they could react directly with the aluminium-bearing minerals in the cement, viz. tricalcium aluminate ( $\text{C}_3\text{A}$ ) or tetracalcium aluminoferrite ( $\text{C}_4\text{AF}$ ), and in presence of water, calcium chloroaluminate, i.e., the so-called Friedel's salt (FS) is formed [5]. In the case of hardened cementitious materials, the chloride ions from

---

\*Dr. Yun Bai. Email: [yun.bai@ucl.ac.uk](mailto:yun.bai@ucl.ac.uk). Tel: +44(0)20 76792386.

\*\* Dr Jing Jing Wang. Email: [JJWANG@tcd.ie](mailto:JJWANG@tcd.ie). Tel: 00353 18964633.

external environments diffuse into the concrete and propagate through the pore solution of concrete [6]. A part of the intruding chlorides is retained by the cement hydrates, through either chemical binding [e.g., formation of FS from monosulphoaluminate (AFm)] [7-9] or physical adsorption [e.g., calcium-silicate-hydrate (C-S-H)] [10], which are named as 'bound chlorides'. The residual chloride ions remain in the pore solution are 'free chlorides', which penetrate through the cover concrete, and when a sufficient amount of chlorides ('critical chloride concentration' or 'threshold value') reaches the reinforcement, a localised breakdown of its passivation film occurs [11]. This then causes the initiation of corrosion of the steel reinforcement. Undoubtedly, chloride induced corrosion is a major deterioration mechanism for reinforced concrete structures exposed to chloride-rich environments, such as marine, de-icing salts and brackish groundwater. However, chloride binding can remove the chloride ions from the pore solution and, thus, delay the initiation of corrosion process. Therefore, understanding the chloride binding, in particular, characterising and monitoring the status of the final binding product, viz. FS, is of great importance to the durability of reinforced concrete structures.

For mature concrete, AFm accommodates the external-chloride to form FS. AFm [7, 12-15] is a lamellar hydrated tetracalcium aluminate-ferrite family that has a representative formula of  $[\text{Ca}_2(\text{Al,Fe})(\text{OH})_6] \cdot \text{X} \cdot \text{nH}_2\text{O}$ , where X refers to a monovalent anion (e.g.,  $\text{OH}^-$ ) or half a divalent charged anion (e.g.,  $\text{SO}_4^{2-}$ ) and n represents the number of water molecules. They belong to Layered Double Hydroxides (LDH) consisting of ordered positively charged rigid main layers  $[\text{Ca}_2(\text{Al,Fe})(\text{OH})_6]^+$  formed by metal ions and hydroxide ions, and negatively charged interlayers  $[\text{X} \cdot \text{nH}_2\text{O}]$  with anions and water molecules. The number of metal cations and hydroxides in the main layer is fixed, while the water and charge-balancing anions in the interlayer space are mobile and replaceable. This intrinsic nature of AFm, actually, defines its anion exchange capacity. In hardened Portland cement paste, AFm forms due to the reaction of ettringite, a product of aluminate minerals ( $\text{C}_3\text{A}/\text{C}_4\text{AF}$ ) in Portland cement and sulphate ( $\text{CaSO}_4 \cdot 2\text{H}_2\text{O}$ ), with  $\text{C}_3\text{A}$ . In commercial cement, very limited Fe(III) substitution of Al occurs in the above reaction and usually only the Al-bearing AFm phase is considered. Besides, the anions in the AFm phase formed within the unaffected cement matrix are originally dominated by  $\text{SO}_4^{2-}$  (sulphate) [7, 12-15]. Hence, for cement chemistry, AFm is represented as  $(\text{Ca}_2\text{Al}(\text{OH})_6 \cdot \text{SO}_3)$  [16]. When concrete is in service condition, the anions accommodated at the inter-layer space are prone to be replaced by other anions. This includes the generally accepted mechanism associated with chemical binding of chlorides in concrete, i.e.,  $\text{Cl}^-$  from external media displaces other anions in AFm to form the Cl-AFm phase, i.e.,  $\text{FS}(\text{Ca}_2\text{Al}(\text{OH})_6(\text{Cl,OH}) \cdot 2\text{H}_2\text{O})$  [17]. Due to this reason, AFm phase has been considered as a 'sink' for chloride ions [17].

Due to its importance, many analytical technologies have been employed to study the FS. The most popular and valuable tool is  $^{27}\text{Al}$  Solid State Nuclear Magnetic Resonance (NMR) Spectroscopy [7, 18-20]. It detects and analyses only one nuclear-spin isotope (e.g.  $^{27}\text{Al}$ ) at a time by employing the nuclear-spin selectivity so that the aluminium chemistry associated with its chemical reaction, composition and local structure is well investigated. In particular, it has demonstrated its unique superiority in analysing Al-bearing phases, such as AFm and FS, as the high sensitivity for  $^{27}\text{Al}$  nucleus (e.g. 100% natural abundance) allows to distinguish easily its tetrahedral and octahedral coordination. Furthermore, the recent development in Magic Angle Spinning (MAS) technique allows the use of MAS probe to obtain well-resolved NMR spectra. Unfortunately, a major disadvantage facing the  $^{27}\text{Al}$  NMR is the effect of the non-spherical charge distribution around the  $^{27}\text{Al}$  nucleus, which can make the spectra interpretation difficult [7, 18-20]. Whilst X-ray Diffraction (XRD) can qualitatively identify the various ionic-groups and the unit-cell parameters of FS [21-23], a high degree of disorder could be an issue for samples containing not perfectly ordered phases. Thermogravimetry (TG)/Differential thermogravimetry analysis (DTG) has been employed to study the mass loss of the FS as a function of increasing temperature, through which the thermo-stability and thermo-chemistry of FS can be illustrated [17, 23, 24]. However, a supplementary analysis is usually conducted jointly as TG cannot provide any fingerprint information for identifying the crystallographic features of FS.

In contrast, vibrational spectroscopy could be a valuable alternative for characterising FS by providing useful information on the molecular composition and symmetry of FS. For example, Fourier Transform Infrared Spectroscopy (FTIR) has been extensively and effectively employed to study the ionic structure of FS, and Table 1 below reports the absorption bands collected by FTIR [17, 25-32]. Evidently, FTIR has demonstrated its unique strength in characterising FS as manifested by its characteristic absorption bands primarily from the  $\text{Al}(\text{OH})_6$  tetrahedral groups and OH bonds.

Table 1 Summary of the IR bands and assignments of Friedel's salt

Phase	FTIR bands / $\text{cm}^{-1}$	Assignments
FS	532, 577	Al-OH stretching vibration mode
	785	Al-OH bending vibration mode
	1621	Water bending vibration mode
	3480	OH stretching region
	3636	(e.g., water stretching vibration, M(metal)-OH stretching mode)

N.B.:  $\text{Cl}^-$  does not absorb in the range  $400\text{-}4000\text{ cm}^{-1}$  due to the ionic nature of chloride bonding.

In addition to FTIR, another advanced vibrational spectroscopy, viz. Raman spectroscopy[33], can also provide 'fingerprint' information of molecular structures for solids, liquids and gases. It works on inelastic scattering that the scattered light occurs at wavelength (frequency) shifted up or down from the incident laser light. As this wavelength shift is specific to the chemical bonds and the symmetry of molecules, Raman scattered signal can thus be used to identify ionic groups in substances. Compared to FTIR, Raman spectroscopy is more appropriate for analysing non-polar molecules, inorganic materials as well as aqueous solutions, and no sample preparation is required. Application of Raman spectroscopy in cement and concrete was first demonstrated by Bensted in 1976 [34], after which various research data have been reported and the main application areas can be grouped as follows:

- i) identification of anhydrous cement/clinker minerals ( $C_3S$ ,  $\beta$ - $C_2S$ ,  $C_3A$  and  $C_4AF$ ) [35, 36], and their hydration phases (CH, C-S-H, AFt and AFm) [35, 37-41];
- ii) characterisation of concrete deterioration products, such as sulphate-bearing phases (i.e. AFt, gypsum and thaumasite) and calcium carbonate polymorphs (i.e. calcite, vaterite and aragonite) [39, 42-48];
- iii) some specific applications such as the study of the structural features of vaterite and C-S-H, characterisation of dehydration mechanism and properties of gypsum under high pressure as well as the phase transformation of  $C_2S$  under high-temperature [49, 50].

It may be noted that the AFm phase, the precursor of FS salt, has already been well studied by Raman spectroscopy in the literature. It has been reported that under Raman spectroscopy, all the internal vibrational modes [i.e. symmetric stretching ( $\nu_1$ ), symmetric bending ( $\nu_2$ ), asymmetric stretching ( $\nu_3$ ) and asymmetric bending ( $\nu_4$ )] of  $SO_4^{2-}$  ionic groups, along with the Al-OH stretching vibration and other external modes, in AFm have been clearly identified [39, 41, 51]. Furthermore, although some research attempted to use Raman spectroscopy characterising LDH phases [15, 30, 31, 52, 53], unfortunately, to date, no comprehensive work has been reported on investigating pure FS and FS in cementitious materials with Raman spectroscopy.

Our current study, hence, seeks to characterise both pure FS (Section 3.1) and the FS formed in cementitious materials (Section 3.2) by using Raman spectroscopy. A FS sample was synthesised under laboratory condition and its phase composition and purity were first assessed by conducting XRD, TG/DTG and FTIR analyses. The FTIR resolved bands obtained were used as one reference for ascribing the Raman bands of FS. Following this, Raman spectroscopy was employed to characterise the pure FS sample and its fingerprint Raman bands were retrieved and assigned. The Raman fingerprint obtained from the pure FS was subsequently employed to recognise the FS formed in a PC paste powder after

being subjected to accelerated chloride attack. The results thus obtained are discussed to establish the potential of Raman spectroscopy for characterising the FS.

## 2. Experimental

### 2.1 Materials

The Portland cement (PC) used in this study was CEM I (in accordance with BS EN 197-1:2011) supplied by QUINN Cement. Its chemical composition is reported in Table 2, and its aluminate contents, i.e. tricalcium aluminate ( $C_3A$ ) and tetracalcium aluminoferrite ( $C_4AF$ ), are 11.31% and 8.98% respectively according to Bogue calculation. The cement pastes were manufactured at a water-to-cement ratio (W/C) of 0.35. After 24 hours' initial curing in plastic tubes, the specimens were removed from the tube and then covered with a water saturated hessian, which were then sealed in plastic sample bags and stored in a curing room at a constant temperature of  $20(\pm 1)^\circ\text{C}$  for around 6 months. This rather long curing duration was purposely selected because in the real world, chloride induced durability issue is mainly occurred in mature concrete. At the end of the sixth month, selected pastes were ground into powder to a fineness of  $63\ \mu\text{m}$ . A 2.8M (165g/L) sodium chloride (NaCl) solution as specified in the NT BUILD 443 was employed in the chloride attack test. The quantity of the solution was determined in accordance with NT BUILD 443, and the solid (g) to liquid ( $\text{dm}^3$ ) ratio was about 1:10. The powder was exposed to the NaCl solution for 14 days which was then filtered and dried in a vacuum chamber.

Table 2 Chemical composition of PC

Oxides	SiO <sub>2</sub>	Al <sub>2</sub> O <sub>3</sub>	Fe <sub>2</sub> O <sub>3</sub>	CaO	MgO	K <sub>2</sub> O	Na <sub>2</sub> O	SO <sub>3</sub>
Content /w%	23.00	6.15	2.95	61.30	1.80	0.68	0.22	2.50

The FS was synthesised under controlled conditions in the laboratory by a coprecipitation method [25, 54]. The two chemicals used for synthesising FS, i.e., calcium chloride ( $\text{CaCl}_2$ ) and sodium aluminate ( $\text{NaAlO}_2$ ), were purchased from Sigma-Aldrich, UK. The  $\text{CaCl}_2$  was anhydrous powder with assay of 99.99% trace metals basis, and the  $\text{NaAlO}_2$  was anhydrous powder with impurities  $\leq 0.05\%$ . First, 300 mL  $\text{CaCl}_2$  (0.5 M) solution was prepared and preheated to  $50^\circ\text{C}$ . Then, 300mL  $\text{NaAlO}_2$  (0.25 M) solution was added into the  $\text{CaCl}_2$  solution at a rate of 5 mL/min, and the mixture was stirred continuously at 300 rpm. After reaction for 1 hour, the precipitate was collected by the filtration, washed three times with

deionised water to remove residual substances and dried in a vacuum chamber. The sample so obtained was ground and then stored in a desiccator for later analyses.

## **2.2 X-ray Diffraction (XRD)**

The powder method of X-ray diffraction was adopted in the present study as a supplementary technique to verify the purity of the FS synthesised and the formation of FS in the PC paste sample. An XPERT-PRO diffractometer with a X-ray source of Co K $\alpha$  radiation ( $\lambda=1.78901$  Å) was used. A scanning speed of 2°/min and step size of 0.017°2 $\theta$  were used to examine the samples in the range of 5° to 70° 2 $\theta$ . The X-ray tube voltage and current were fixed at 40 kV and 30 mA respectively.

## **2.3 Fourier transform infrared spectroscopy (FTIR)**

The FTIR spectra were collected on a FTIR spectrometer in the range of 500-4000 cm<sup>-1</sup> with a resolution of 1 cm<sup>-1</sup> at ambient temperature under a transmission mode.

## **2.4 Thermogravimetry(TG)/Differential thermogravimetry(DTG) analysis**

Thermogravimetric (TG) analysis was performed with a NETZSCH STA 449C instrument under N<sub>2</sub> environment. The DTG trace was recorded simultaneously. The tests were carried out between 25°C and 1000 °C with a heating rate of 20 K/min.

## **2.5 Raman spectroscopy**

The Raman analysis was performed under back-scattering geometry on a Renishaw Invia micro-Raman spectrometer equipped with a Charged Coupled Device (CCD) detector. A 514.5nm single-line (Argon ions) laser with an output power of 25mW was employed as the excitation source. The laser beam was focused into a laser spot about 1.26  $\mu$ m diameter by means of a LEICA Plan N objective with 50X magnification, and then interrogated the sample. Measured power at the sampling level was around 4.1 mW. The Raman shift was calibrated before each experiment using the sharp peak of silicon at 520 cm<sup>-1</sup>. Raman spectra were recorded with an exposure time of 10s and accumulations of 10 to improve the signal-to-noise ratio (SNR). The Raman data were analysed with the employment of the software OriginPro 8.6 (Origin, USA). To eliminate the troublesome background, baseline

correction using OriginPro 8.6 was conducted first to subtract the background (e.g. fluorescence). After removing the background, those Raman peaks obscured previously by the fluorescence could now be clearly observed. The Raman peaks were then fitted with Lorentz function in order to retrieve the peak wavenumber for differentiating the analytes.

### **3. Results and discussion**

As aforementioned, the synthesised pure FS was characterised first in order to establish bench-mark Raman features for identifying the FS formed in cementitious materials. To obtain the genuine Raman spectrum of FS, the XRD and TG/DTG analyses were firstly conducted to verify the phase-composition and purity of the synthesised sample obtained. Besides, FTIR analysis was carried out in order to collect the IR-active vibrational information as a reference for assigning the Raman bands of FS later. The Raman features of the pure FS were first collected and attributed. Building upon this, the chloride attacked PC paste powder was investigated and the Raman fingerprint of the FS phase formed was then identified and assigned accordingly.

#### **3.1 Pure Friedel's salt**

##### **3.1.1 Verification of synthesised FS**

###### **3.1.1.1 XRD analysis**

The XRD pattern of the synthesised FS is presented in Fig. 1, which matches well with the standard JCPDS card No. 00-019-0201. As shown in the figure, the typical XRD peaks of FS (e.g.  $2\theta = 13.2^\circ$ ,  $26.5^\circ$ ,  $27.3^\circ$  and  $36.5^\circ$ ) were identified in the synthesised phase, indicating the formation of the FS crystals in this sample. Furthermore, as those intense peaks dominate the XRD diffractogram, it could be concluded that the FS synthesised here under laboratory conditions has a high purity (to be further confirmed in the following section). At the same time, tiny amount of halite (NaCl) and gibbsite ( $\text{Al}(\text{OH})_3$ ) have also been identified in this synthesised sample, which could be generated by the associated reactions between the raw chemicals (e.g.  $\text{CaCl}_2$  and  $\text{NaAlO}_2$ ) used during the synthesis processes.

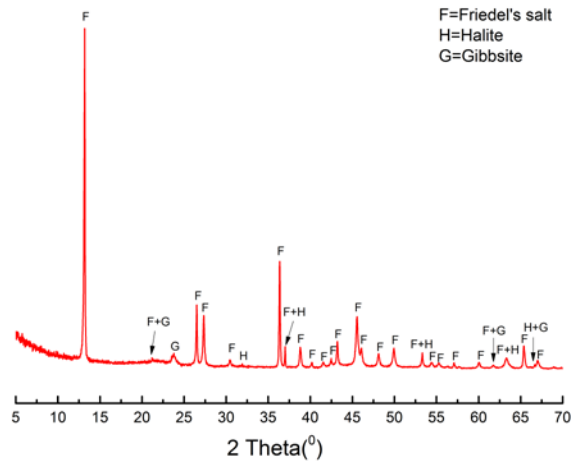


Fig.1 XRD pattern of synthesised Friedel's salt

### 3.1.1.2 TG/DTG analysis

Fig.2 reports the TG (weight loss) and DTG curves of the FS. Evidently, ordered crystalline structure of FS yielded a well-revolved TG curve with three weight-loss steps, which can be used to verify the composition of the synthesised FS, as described below [17, 23, 24]:

- (i) Weight loss between 25 - 200 °C: A peak at about 135 °C can be clearly observed, in DTG curve. This weight-loss is due to the removal of the water molecules in the interlayer space and this dehydration process may give rise to a product with reduced crystallinity, i.e.  $3\text{Ca}(\text{OH})_2 \cdot 2\text{Al}(\text{OH})_3 \cdot \text{CaCl}_2$  [17].
- (ii) Weight loss between 200 – 400 °C: At this temperature range, there were two peaks seen at about 260 °C and 340 °C respectively, corresponding to the dehydroxylation of the main portlandite-like sheets, leading to the formation of a poorly structured phase.
- (iii) Weight loss between 400-1000 °C: This weak effect could be caused by various phase transformations, such as the recrystallisation of the amorphous phase (above ca 750 °C), yielding a mixture of CaO and mayenite ( $\text{Ca}_{12}\text{Al}_{14}\text{O}_{33}$ ) [23], or the release of water from recombination of hydroxyl groups or probably anion decomposition.

Based on the calculation, the weight loss in the abovementioned three steps are 11.5 %, 18.2 % and 8.0 % respectively, which is consistent with the findings obtained from typical FSs as reported in the literature [23]. Moreover, a total weight loss of about 38% can be obtained, and this result matches well with the theoretical water content of an idealised FS formula, i.e. around 32.1 %.

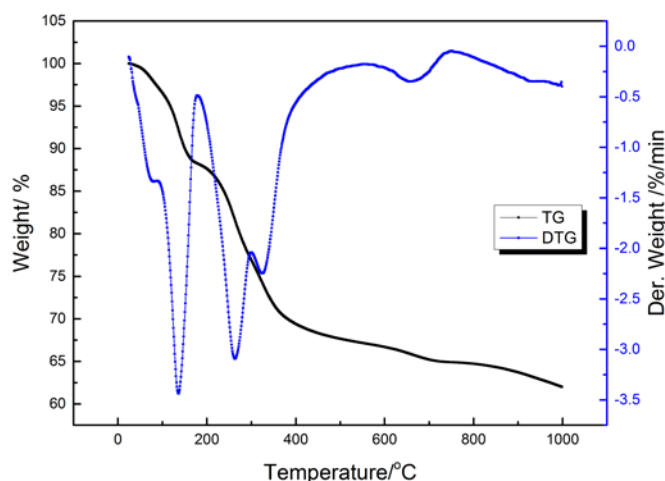


Fig.2 TG and DTG analysis of synthesised Friedel's salt

### 3.1.1.3 FTIR analysis

Fig. 3 depicts the IR spectrum of the synthesised FS sample and its various absorption bands can be assigned according to the information reported in literature [17, 25-31], as described next. The strong overlapping at the high frequency area, i.e.  $3484\text{ cm}^{-1}$  and  $3628\text{ cm}^{-1}$ , could be the OH stretching region associated with the water stretching vibration and the M(metal)-OH stretching mode of the hydroxide layer. The band at  $1621\text{ cm}^{-1}$  is the H-O-H bending vibration of interlayer water. At the same time, the bands at low wavenumber area, i.e.  $788\text{ cm}^{-1}$  and  $530/585\text{ cm}^{-1}$ , are characteristics of the bending vibration and stretching vibration modes of the Al-OH bonds of  $\text{Al}(\text{OH})_6$  octahedra respectively. In addition, the band identified at  $878\text{ cm}^{-1}$  and  $1440\text{ cm}^{-1}$  are caused by the out-of-plane bending ( $\nu_2$ ) and asymmetric stretching ( $\nu_3$ ) vibration of  $\text{CO}_3^{2-}$  groups in carbonate phase in the sample [30, 32, 53], which could be formed during the sample preparation. There are some minor bands observed in the spectrum, which could be attributed to the impurities in the raw materials used to synthesise the FS. It should be noted that no vibrational bands of chloride ions in the range of  $400 - 4000\text{ cm}^{-1}$  were identified due to the ionic nature of the chloride bonding [17].

Therefore, based on the FTIR, TG/DTG and XRD results, it could be concluded that FS phases with reasonable crystallographic compositions and dominant proportion have been formed in the synthesised FS product. This FS was then used in the following Raman spectroscopy analysis.

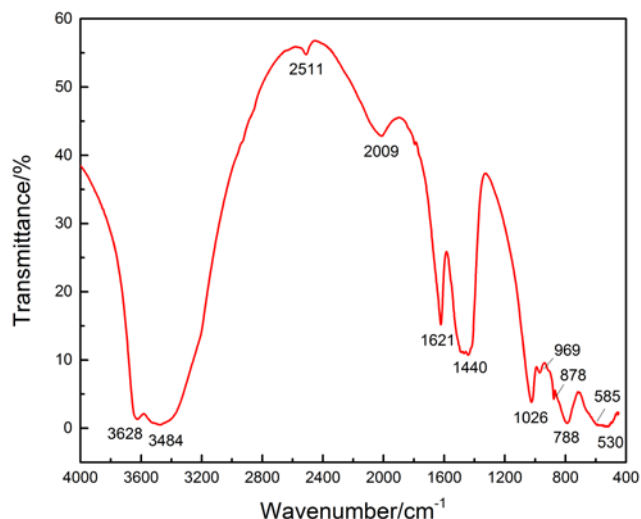


Fig.3 FTIR spectrum of synthesised Friedel's salt

### 3.1.2 Raman spectroscopy analysis

#### 3.1.2.1 Raman spectra of FS and bands assignment

As mentioned above, until now no comprehensive research conducted on Raman spectroscopy study of either the pure FS or the FS formed in cement matrix. Hence, in the current study, the synthesised pure FS was analysed first so that the Raman bands retrieved and assigned can be used as bench-mark to analyse the FS formed in the PC paste sample later. In this study, in order to clearly identify all the possible molecular vibration modes in the synthesised FS, extended scan mode between  $200\text{ cm}^{-1}$  and  $4000\text{ cm}^{-1}$  was employed in an attempt to record all the detectable Raman bands. Fig. 4 represents the full Raman spectrum of the synthesised FS under extended scan mode. In the original spectrum Fig. 4(a), an unwanted sloping background was observed from  $200\text{ cm}^{-1}$  onwards which may hamper the genuine Raman peaks. This background could be the troublesome fluorescence induced by the uncertain impurities in the raw materials used to synthesise the FS. Hence, baseline correction using OriginPro 8.6 was applied to eliminate the background effect and the resultant spectrum is presented in Fig. 4(b).

Obviously, as shown in Fig. 4(b), the Raman bands of FS were located mainly at two frequency regions, i.e. low frequency range ( $200\text{--}1200\text{ cm}^{-1}$ ) and high frequency range ( $3200\text{--}3800\text{ cm}^{-1}$ ). From FTIR bands assignment summarised in Table 1, the IR-active vibrations of the functional group  $\text{Al}(\text{OH})_6$  octahedra is located at the low-wavenumber range, whilst the high frequency bands are mostly attributable to the water and hydrogen bond network. Hence, these two Raman frequency ranges are discussed separately below.

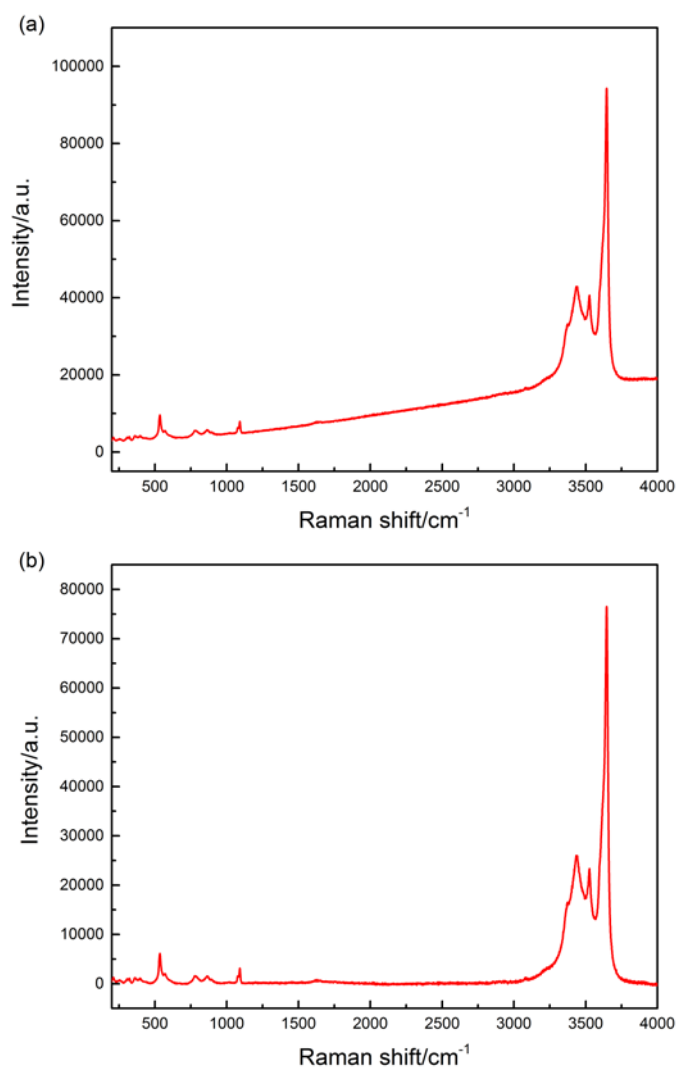


Fig.4 Raman spectra of synthesised Friedel's salt (200-4000  $\text{cm}^{-1}$ ). (a) Original spectrum. (b) Spectrum after subtracting background

#### a) Low frequency range (200-1800 $\text{cm}^{-1}$ )

The Raman spectrum (after subtracting background) of FS recorded between 200  $\text{cm}^{-1}$  - 1800  $\text{cm}^{-1}$  is presented in Fig. 5. Several Raman peaks can be clearly observed in this background-subtracted spectrum in this low wavenumber range.

In Fig. 5, the most intense and well-defined peak emerged at 534  $\text{cm}^{-1}$ , as well as its shoulder at 568  $\text{cm}^{-1}$ , are unique in FS representing the stretching vibration mode of Al-OH bonds in the  $\text{Al}(\text{OH})_6$  octahedra. Furthermore, an adjacent band visible at 783  $\text{cm}^{-1}$  could be attributed to the Al-OH bending vibration mode [17, 30]. Some minor bands at 200-500  $\text{cm}^{-1}$  were also identified, i.e. the bands at 212  $\text{cm}^{-1}$  and 255  $\text{cm}^{-1}$  (external rotation and translation), and 362/397  $\text{cm}^{-1}$  (Ca-O stretching vibration) [30]. Besides, the hump located at 1629  $\text{cm}^{-1}$  could be assigned to

the H-O-H bending vibration of water molecules in the FS [17, 31, 55]. It is worthwhile to note that, instead of calcite the vaterite phase was identified in this sample as evidenced by its various Raman bands, i.e., the sharp peaks at  $1077\text{ cm}^{-1}$  and  $1092\text{ cm}^{-1}$  ( $\nu_1\text{CO}_3$  symmetric stretching vibration),  $868\text{ cm}^{-1}$  ( $\nu_2\text{CO}_3$  out-of-plane bending) and  $305/323\text{ cm}^{-1}$  (lattice vibration)[53, 56, 57].The formation of vaterite in the current sample could be due to the carbonation occurred during the sample preparation or storage under relatively dry environment, which is in good agreement with the literature [49, 57, 58].

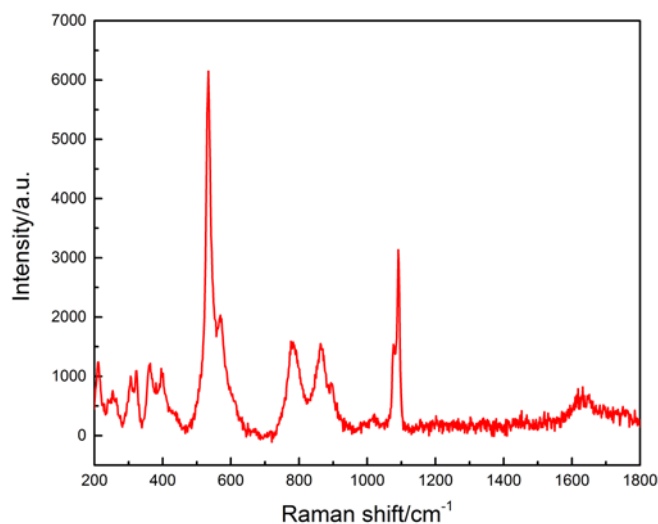


Fig.5 Raman spectrum of synthesised Friedel's salt in low frequency range (200-1800  $\text{cm}^{-1}$ )

### **b) High frequency range (1800-4000 $\text{cm}^{-1}$ )**

The Raman spectrum (after subtracting background) of FS in the high wavenumber range is reported in Fig. 6. Obviously, contrary to the hydrogen bond in normal water which shows an extremely broad hump with strongly-overlapping bands at the wavenumber range of  $3200\text{-}3800\text{ cm}^{-1}$ , the hydrogen bond in the FS led to well-resolved peaks at high frequency range. More importantly, this spectrum range from  $3200\text{-}3800\text{ cm}^{-1}$  represented two different hydrogen bond network in FS. The broad band on the left-side (at about  $3200\text{-}3600\text{ cm}^{-1}$ ), with three well-resolved peaks at  $3432\text{ cm}^{-1}$ ,  $3527\text{ cm}^{-1}$  and  $3617\text{ cm}^{-1}$ , corresponds to the stretching of water molecules in the interlayer. On the other hand, the intense and sharp peak identified at  $3646\text{ cm}^{-1}$ , was from the stretching of hydroxyl groups [30, 56, 59-61]. This phenomenon indicates the much ordered arrangement of the hydroxyls over the water molecules. Indeed in the FS, the hydroxyls in the main-layers are perfectly coordinated with bridge  $\text{Cl}^-$  ions and participated to the cohesion of the lamellar structure. However, there is a dynamic disorder in the interlayer part of the FS structure, and, hence, the water molecules have much high freedom.

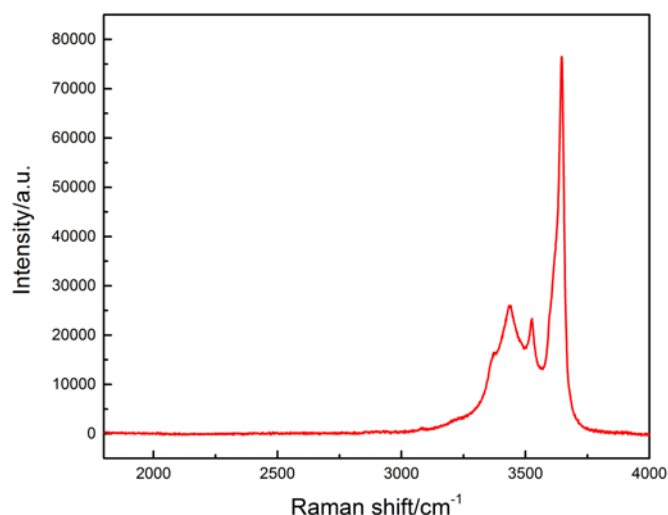


Fig.6 Raman spectrum of synthesised Friedel's salt in high frequency range (1800-4000  $\text{cm}^{-1}$ )

### 3.1.2.2 Discussion

In the above Section, the various Raman bands correspond to the functional groups of FS have been identified and assigned. In this section, attempts have been made to try to understand the possible relationship between the identified Raman vibrational information and the change incurred to the composition and structure of the interlayer when AFm was converted to FS in the presence of chloride ions. The structure of the FS, especially, the local structural information associated with the  $\text{Cl}^-$  ions is discussed in detail first. Building upon this, the Raman bands of FS are compared to those of AFm, in order to understand the effect that the incorporation of chloride ions might have on the structure and, consequently, the Raman bands, of FS.

#### a) Structure of FS and its Cl-site

FS [7, 18, 21, 60-63], also known as hydrocalumite or Cl-AFm, has a unique crystal structure amongst Layered Double Hydroxide (LDH) family and is the only member that a single crystal structure refinement is available. As introduced in Section 1, FS forms by replacing the anions ( $\text{SO}_4^{2-}$ ) at the inter-layer space of AFm by  $\text{Cl}^-$  ions. Its crystallographic structure can be described by periodically stacking of the positively charged main layers  $[\text{Ca}_2\text{Al}(\text{OH})_6]^+$  and negatively charged interlayers  $[\text{Cl}^-, 2\text{H}_2\text{O}]$ . The main layer demonstrates a portlandite-like structure, i.e. every third  $\text{Ca}^{2+}$  cations in the octahedral sites in principle hydroxide layer are replaced by  $\text{Al}^{3+}$  ions to form a permanent positive charge. This charge is neutralised by the compensating anions,  $\text{Cl}^-$ , in the interlayer space. Similar to AFm compounds, the  $\text{Al}^{3+}$  and  $\text{Ca}^{2+}$  cations are coordinated by six- and seven-oxygen (O) respectively. The chloride

anion, introduced into the middle-space of two adjacent main layers, is just suited in the centre of an octahedral cavity formed by O(w) atoms from water molecules. Fig.7 shows the environment of a chloride anion in the interlayer of the FS [62-65]. Apparently, a chloride ion is hydrogen-bonded to 10 neighbouring H-atoms, i.e. six from hydroxyl groups (three each from two adjacent main layers) and four from water molecules. The hydroxyls in the main-layers are coordinated with cations, e.g., Al is coordinated to six hydroxyl groups in the main layer [18]. The water molecules are on the other hand bonded to the  $\text{Ca}^{2+}$  cations in the main-layer viz. each  $\text{Ca}^{2+}$  is approached by the seventh O(w)-atom presents in the interlayer region. Hence, the so-formed hydrogen bond network bridges the  $\text{Ca}^{2+}$  ions, water molecules and  $\text{Cl}^-$  anions following: Ca (main layer)...O(w)-H(w) (interlayer)...Cl (interlayer)...H(w)-O(w) (interlayer)...Ca (main layer) ensuring the connection between main layers and interlayers. This symmetric hydrogen bond network keeps chloride ions virtually immobile even at temperature as high as  $300^\circ\text{C}$ . Furthermore, this H-bond arrangement around the  $\text{Cl}^-$  site affects the properties of FS significantly. It is reported that the phase transition of FS at temperature above  $35^\circ\text{C}$ , from a monoclinic (m) low-temperature (LT) polymorph (C2/c) to a rhombohedral (rh) high-temperature (HT) polymorph [R3C], is probably due to the altering of hydrogen bond network leading to a decrease of the unit cell volume [18, 21, 66].

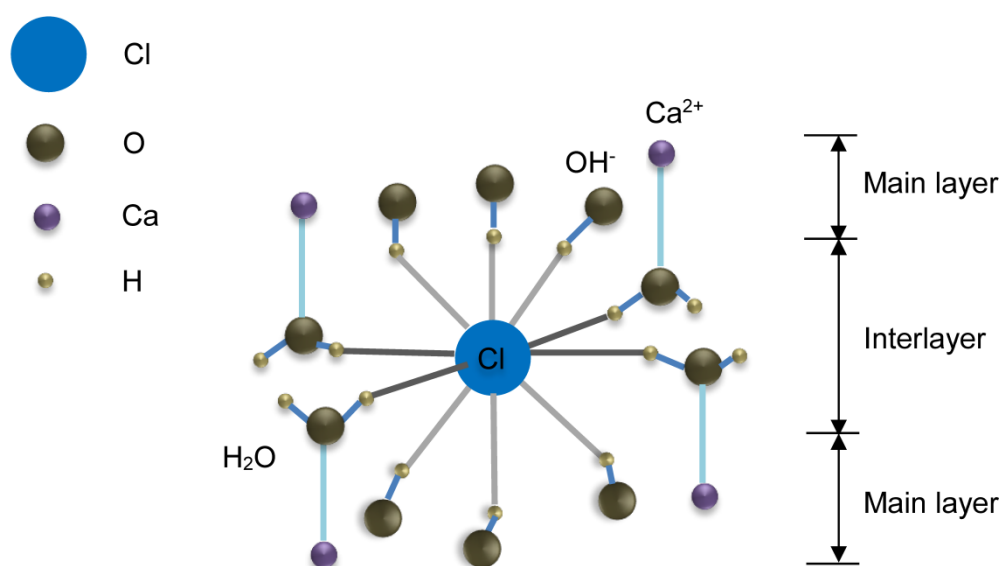


Fig.7 Schematic of the Cl-site in Friedel's salt

## b) Featured Raman bands of FS

Table 3 presents the Raman bands recorded from FS, along with those of AFm phase reported [39] for comparison purpose. Apparently, by comparing the Raman bands of FS

here (first column) and its FTIR bands (Table 1), Raman spectroscopy provides much more vibrational information than FTIR, as evidenced by the vibration bands collected at low-frequency range, i.e. 212/255  $\text{cm}^{-1}$  (the external rotation/translation band) and 362/397  $\text{cm}^{-1}$  (Ca-O stretching).

Table 3 Raman bands of synthesised Friedel's salt and AFm phases

FS	Vibrational modes	AFm
Raman shift / $\text{cm}^{-1}$		Raman shift
212, 255	External rotation and translation	215
362, 397	Ca-O stretching vibration	360
534/568	Al-OH stretching vibration	531
783	Al-OH bending vibration	
305,323	Lattice vibration in vaterite	
868	Out-of-plane bending vibration ( $\nu_2\text{CO}_3$ ) in vaterite	
1077, 1092	Symmetric stretching vibration ( $\nu_1\text{CO}_3$ ) in vaterite	
1629	Water bending vibration mode	
3646	OH stretching of hydroxyl	3678
3432, 3527, 3617	OH stretching of water molecules	3416, 3221
	Symmetric stretching vibration ( $\nu_1\text{SO}_4$ )	983
	Asymmetric stretching vibration ( $\nu_3\text{SO}_4$ )	1114
	Symmetric bending vibration ( $\nu_2\text{SO}_4$ )	396,447
	Asymmetric bending vibration $\nu_4(\text{SO}_4)$	614

From Table 3, it can be seen that there are distinct differences in the Raman bands between FS and AFm, which could be possibly attributed to the following reasons:

- i) Disappearance of  $\text{SO}_4^{2-}$  ionic groups. The Raman features of  $\text{SO}_4$  ionic-units in AFm were absent from the FS, which is fully consistent with the anion-exchange in FS viz. the  $\text{SO}_4^{2-}$  ions are replaced by  $\text{Cl}^-$ ;
- ii) Incorporation of chloride ions and subsequent modification to the local structure of  $\text{Al}(\text{OH})_6$  octahedra. Evidently, at the Raman wavenumber range 500-800  $\text{cm}^{-1}$ , corresponding to the vibration bands of  $\text{Al}(\text{OH})_6$  octahedra, there were different Raman features in FS compared to AFm. Firstly, in FS a shoulder was observed at 568  $\text{cm}^{-1}$  adjacent to the peak at 534  $\text{cm}^{-1}$  (Al-OH stretching vibration), which is different from the AFm where only a single peak exhibited at 531  $\text{cm}^{-1}$ . In addition, there was a new Al-OH vibration mode emerged at 783  $\text{cm}^{-1}$  in FS over AFm. This Raman-active band, equivalent to the FTIR band observed at 788  $\text{cm}^{-1}$ , represents the Al-OH bending vibration. The emergence of this Al-OH bending vibration band in the Raman spectrum of FS, as well as the shoulder of the Al-OH stretching vibration, could be caused by the alteration of the

local site of  $\text{Al}(\text{OH})_6$  octahedral units due to the substitution of  $\text{Cl}^-$  for  $\text{SO}_4^{2-}$  ions. As aforementioned,  $\text{Cl}^-$  located at the interlayer is directly hydrogen-bonded to six hydroxyl groups in the main-layers. Meantime, these  $\text{OH}^-$  are coordinated to the cations, either  $\text{Al}^{3+}$  or  $\text{Ca}^{2+}$ , to form the rigid ionic units such as  $\text{Al}(\text{OH})_6$  octahedra. Hence, for FS, the incorporation of  $\text{Cl}^-$  ions for replacing original  $\text{SO}_4^{2-}$  could change the bonding environment and subsequently the site structure of  $\text{Al}(\text{OH})_6$  octahedra, leading to the emergency of the new vibrational features.

Besides, the high frequency Raman range gave an insight into the hydrogen bond network in the water molecules and hydroxyls. This feature is quite similar to that from FTIR.

## 3.2 Friedel's salt in cementitious materials

### 3.2.1 Verification of the formation of FS by XRD

The chloride attacked sample was first analysed by XRD in order to clarify the formation of the FS in the deteriorated PC sample. Fig.8 represents the XRD pattern of the chloride attacked PC paste sample.

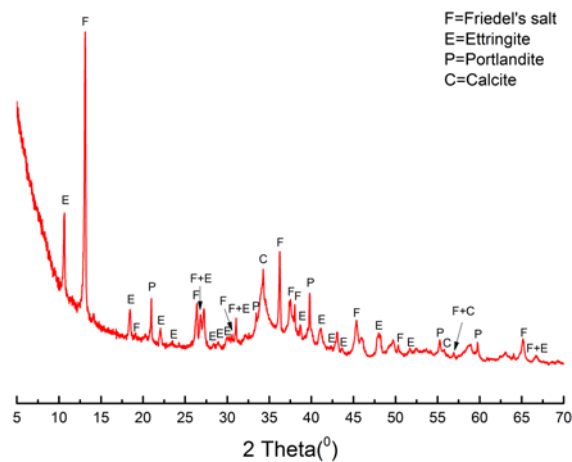


Fig.8 XRD pattern of chloride attacked PC paste sample

As shown in Fig. 8, FS has been formed in the cement paste exposed to chloride solution, as indicated by its XRD peaks located at  $2\theta = 13.1, 26.4, 27.3$  and  $36.2^\circ$ . At the same time, various cement hydration products have also been identified, such as ettringite ( $2\theta = 10.7, 18.5$  and  $22.0^\circ$ ) and portlandite ( $2\theta = 21.0, 33.4$  and  $39.8^\circ$ ). Furthermore, there were some humps, such as those at about  $2\theta = 46\sim 47$  and  $48\sim 50^\circ$ , cannot be assigned. These humps could be attributed to the calcium silicate hydrate (C-S-H) phases formed under the

hydration of Cement I - they could not give sharp XRD peak due to their poorly crystalline structures. Moreover, calcite is identified in the cement sample which could have been formed from the carbonation during sample preparation. Hence, it can be confirmed that FS crystals were formed in the chloride attacked PC paste samples.

### 3.2.2 Raman spectroscopy analysis

As discussed in Section 3.1, the synthesised pure FS can be readily identified under Raman spectroscopy. However, whilst the Raman bands of pure and white coloured FS salt can be easily identified, it could potentially be difficult to characterise FS salt in the chloride attacked cement paste due to the following reasons:

- i) the grey colour of PC paste sample. As Raman signal is basically occurred on the principle of scattering, grey colour could possibly reduce the signal because of its potential absorption effect to the excitation laser;
- ii) the heterogeneous nature of cementitious materials. Due to the fact that the laser-sampling spot of Raman spectroscopy is only at micron-scale, i.e. 1.26  $\mu\text{m}$  diameter, it could be difficult to retrieve a holistic view of the samples;
- iii) the potential of strong fluorescence. The impurities existed in the cement (e.g. organic compound), the defects introduced during grinding and the inter-particle scattering could cause strong fluorescence background to the intrinsically weak Raman peaks [37], which can impose disturbance to or even totally hamper the weak Raman peaks.

Fig. 9(a) shows the Raman spectrum of the chloride attacked PC sample. As the Raman feature of FS is mainly located at the Raman shift of 500 – 800 $\text{cm}^{-1}$ , only a Raman region between 200 and 1700  $\text{cm}^{-1}$  is reported.

As illustrated in Fig. 9(a), strong sloping backgrounds, as expected, were emerged from 200  $\text{cm}^{-1}$  onwards in the spectrum. These could be the unwanted fluorescence as aforementioned. Hence, the background was again subtracted and the resultant spectrum is presented in Fig. 9(b). The most intense doublet at 513/536  $\text{cm}^{-1}$  could be attributed to the stretching vibration mode of Al-OH in the aluminite-bearing phases, such as the FS and AFm minerals. Besides, Al-OH bending mode was also recognised as manifested by the Raman band at 740  $\text{cm}^{-1}$ . Additionally, there were two peaks identified at the low frequency region, i.e. 245  $\text{cm}^{-1}$  and 356  $\text{cm}^{-1}$ , which could be due to the external rotation/translation and Ca-O stretching vibration mode respectively. Furthermore, a vibration band was also observed at 673  $\text{cm}^{-1}$ , which could be associated with the Si-O-Si symmetric bending vibration of C-S-H phase [67], whilst the peak at 988  $\text{cm}^{-1}$  of the symmetric stretching

vibration of ( $\nu_1$  SO<sub>4</sub>) could be attributed to calcium aluminate monosulphate (AFm) phases. The carbonate band emerged again at 1076 cm<sup>-1</sup> [ $\nu_1$  (CO<sub>3</sub>)]. In addition, the hump located at 1607 cm<sup>-1</sup> represents the H-O-H bending vibration of water molecules in FS salt was also recognised. The above results indicate that the typical Raman bands of FS salt formed in the chloride attacked PC paste have been recognised by Raman spectroscopy, confirming fully the potential of Raman for distinguishing the FS formed in cementitious materials.

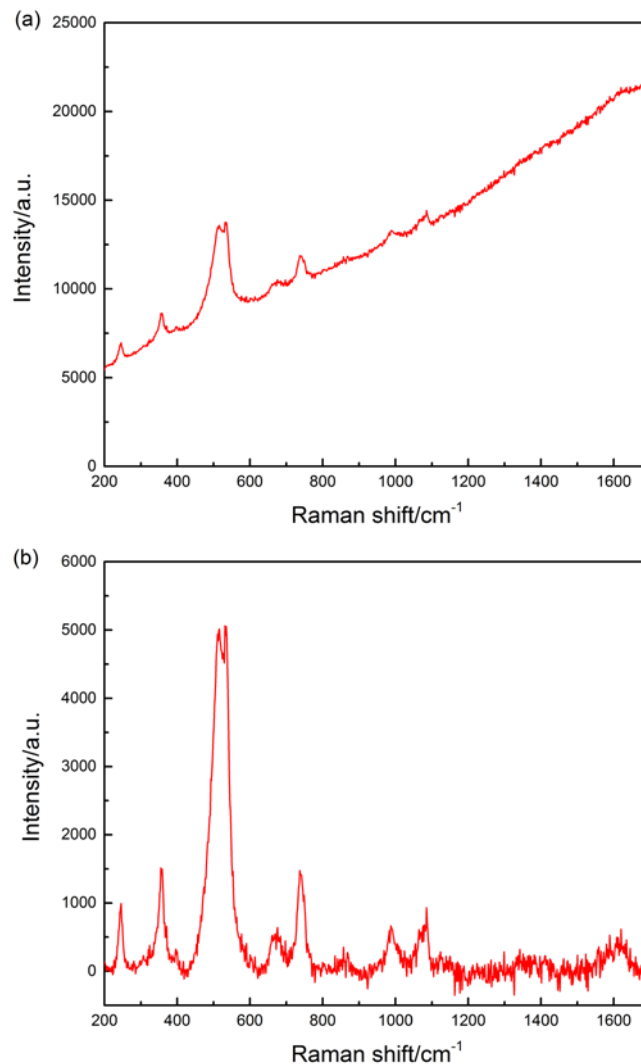


Fig.9 Raman spectra of chloride attacked PC paste sample. (a) Original spectrum. (b) Spectrum after subtracting background

Moreover, by comparing Fig. 5 and Fig. 9(b), it becomes evident that different Raman-band features were retrieved from the pure FS and the cement paste sample. Taking the Al-OH stretching band as an example, wavenumber-shift and band splitting were observed, and these bands were very strong. In pure FS, a sharp peak (534 cm<sup>-1</sup>) and a shoulder (568 cm<sup>-1</sup>) were identified. However, from the chloride attacked PC paste sample, an intense doublet

was recognised at 513/536  $\text{cm}^{-1}$ . This could be due to the complex nature of the cementitious matrix. On the other hand, there could be more than one AFm phases existing in the current cement matrix which could also contribute to the Al-OH stretching vibration, resulting in enhanced Raman bands.

## 4. Conclusions

Friedel's salt (FS) forms upon chloride binding with monosulphoaluminate (AFm) phase. By characterising the FS formed under chloride attack, we can obtain useful information on the chloride binding capacity of concrete, which will eventually facilitate the prediction of service life of reinforced concrete structures. So far, there is no comprehensive research on the application of Raman spectroscopy for studying FS. In the current study, a full Raman spectrum of pure FS between 200 ~ 4000  $\text{cm}^{-1}$  was successfully obtained, including the featured Raman bands at 534/568  $\text{cm}^{-1}$  and 783  $\text{cm}^{-1}$  which correspond to the Al-OH stretching and bending vibration of FS, respectively, as can be expected and inferred from the molecular structure of FS. Furthermore, similar Raman bands of FS were identified in a PC paste sample subjected to accelerated chloride attack, further confirming the potential of Raman spectroscopy for distinguishing FS in cementitious materials.

## Acknowledgements

The authors would like to acknowledge the support received from the EPSRC UK-China Science Bridge project, China Scholarship Council and Faculty of Engineering Postgraduate Research Scholarship at University College London (UCL). Appreciation is also extended to Dr. Steve Firth from Department of Chemistry at UCL for his assistance in experiment work. The CEM I Portland cement used in this research was supplied by Quinn Cement.

## References

- [1] A.M. Neville, Properties of concrete, fifth ed., Prentice Hall, San Francisco, 1995.
- [2] H. Song, C. Lee, M. Jung, K. Ann, Development of chloride binding capacity in cement pastes and influence of the pH of hydration products, *Can. J. Civil Eng.* 35 (2008) 1427-1434.
- [3] C. Arya, N. Buenfeld, J. Newman, Factors influencing chloride-binding in concrete, *Cem. Concr. Res.* 20 (1990) 291-300.

- [4] L. Tang, N. Lars-Olof, Chloride binding capacity and binding isotherms of OPC pastes and mortars, *Cem. Concr. Res.* 23 (1993) 247-253.
- [5] A. Neville, Chloride attack of reinforced concrete: an overview, *Mater. Struct.* 28 (1995) 63.
- [6] Q. Yuan, C. Shi, G. De Schutter, K. Audenaert, D. Deng, Chloride binding of cement-based materials subjected to external chloride environment—a review, *Constr. Build. Mater.* 23 (2009) 1-13.
- [7] M. Jones, D. Macphee, J. Chudek, G. Hunter, R. Lannegrand, R. Talero, S. Scrimgeour, Studies using  $^{27}\text{Al}$  MAS NMR of AFm and AFt phases and the formation of Friedel's salt, *Cem. Concr. Res.* 33 (2003) 177-182.
- [8] K. De Weerd, D. Orsáková, M. Geiker, The impact of sulphate and magnesium on chloride binding in Portland cement paste, *Cem. Concr. Res.* 65 (2014) 30-40.
- [9] M. Florea, H. Brouwers, Chloride binding related to hydration products: Part I: Ordinary Portland Cement, *Cem. Concr. Res.* 42 (2012) 282-290.
- [10] J.J. Beaudoin, V.S. Ramachandran, R.F. Feldman, Interaction of chloride and C-S-H, *Cem. Concr. Res.* 20 (1990) 875-883.
- [11] G. Glass, N. Buenfeld, The presentation of the chloride threshold level for corrosion of steel in concrete, *Corros. Sci.* 39 (1997) 1001-1013.
- [12] F. Glasser, A. Kindness, S. Stronach, Stability and solubility relationships in AFm phases: Part I. Chloride, sulfate and hydroxide, *Cem. Concr. Res.* 29 (1999) 861-866.
- [13] T. Matschei, B. Lothenbach, F. Glasser, The AFm phase in Portland cement, *Cem. Concr. Res.* 37 (2007) 118-130.
- [14] L.G. Baquerizo, T. Matschei, K.L. Scrivener, M. Saeidpour, L. Wadsö, Hydration states of AFm cement phases, *Cem. Concr. Res.* 73 (2015) 143-157.
- [15] G. Renaudin, A. Mesbah, B. Zeleke Dilnesa, M. Francois, B. Lothenbach, Crystal chemistry of iron containing cementitious AFm layered hydrates, *Curr. Inorg. Chem.* 5 (2015) 184-193.
- [16] J.P. Skalny, J. Marchand, I. Odler, *Sulfate Attack on Concrete*, Taylor & Francis Group, 2003.
- [17] U. Birnin-Yauri, F. Glasser, Friedel's salt,  $\text{Ca}_2\text{Al}(\text{OH})_6(\text{Cl}, \text{OH})\cdot 2_2\text{O}$ : its solid solutions and their role in chloride binding, *Cem. Concr. Res.* 28 (1998) 1713-1723.
- [18] M.D. Andersen, H.J. Jakobsen, J. Skibsted, Characterization of the  $\alpha$ -  $\beta$  Phase Transition in Friedel's Salt ( $\text{Ca}_2\text{Al}(\text{OH})_6\text{Cl}\cdot 2\text{H}_2\text{O}$ ) by Variable-Temperature  $^{27}\text{Al}$  MAS NMR Spectroscopy, *J. Phys. Chem. A.* 106 (2002) 6676-6682.
- [19] G. Paul, E. Boccaleri, L. Buzzi, F. Canonico, D. Gastaldi, Friedel's salt formation in sulfoaluminate cements: A combined XRD and  $^{27}\text{Al}$  MAS NMR study, *Cem. Concr. Res.* 67 (2015) 93-102.

- [20] J. Chudek, G. Hunter, M. Jones, S. Scrimgeour, P. Hewlett, A. Kudryavtsev, Aluminium-27 solid state NMR spectroscopic studies of chloride binding in Portland cement and blends, *J. Mater. Sci.* 35 (2000) 4275-4288.
- [21] J.-P. Rapin, G. Renaudin, E. Elkaim, M. Francois, Structural transition of Friedel's salt  $3\text{CaO}\cdot\text{Al}_2\text{O}_3\cdot\text{CaCl}_2\cdot 10\text{H}_2\text{O}$  studied by synchrotron powder diffraction, *Cem. Concr. Res.* 32 (2002) 513-519.
- [22] R. Talero, L. Trusilewicz, A. Delgado, C. Pedrajas, R. Lannegrand, V. Rahhal, R. Mejía, S. Delvasto, F. Ramírez, Comparative and semi-quantitative XRD analysis of Friedel's salt originating from pozzolan and Portland cement, *Constr. Build. Mater.* 25 (2011) 2370-2380.
- [23] L. Vieille, I. Rousselot, F. Leroux, J.-P. Besse, C. Taviot-Guého, Hydrocalumite and its polymer derivatives. 1. Reversible thermal behavior of Friedel's salt: a direct observation by means of high-temperature in situ powder X-ray diffraction, *Chem. Mater.* 15 (2003) 4361-4368.
- [24] R.O. Grishchenko, A.L. Emelina, P.Y. Makarov, Thermodynamic properties and thermal behavior of Friedel's salt, *Thermochim. Acta.* 570 (2013) 74-79.
- [25] D. Zhang, Y. Jia, J. Ma, Z. Li, Removal of arsenic from water by Friedel's salt (FS:  $3\text{CaO}\cdot\text{Al}_2\text{O}_3\cdot\text{CaCl}_2\cdot 10\text{H}_2\text{O}$ ), *J. Hazard. Mater.* 195 (2011) 398-404.
- [26] Y. Dai, G. Qian, Y. Cao, Y. Chi, Y. Xu, J. Zhou, Q. Liu, Z.P. Xu, S. Qiao, Effective removal and fixation of Cr (VI) from aqueous solution with Friedel's salt, *J. Hazard. Mater.* 170 (2009) 1086-1092.
- [27] Y. Shao, M. Zhou, W. Wang, H. Hou, Identification of chromate binding mechanisms in Friedel's salt, *Constr. Build. Mater.* 48 (2013) 942-947.
- [28] M. Domínguez, M.E. Pérez-Bernal, R.J. Ruano-Casero, C. Barriga, V. Rives, R.A. Ferreira, L.D. Carlos, J. Rocha, Multiwavelength luminescence in lanthanide-doped hydrocalumite and mayenite, *Chem. Mater.* 23 (2011) 1993-2004.
- [29] Y. Wu, Y. Chi, H. Bai, G. Qian, Y. Cao, J. Zhou, Y. Xu, Q. Liu, Z.P. Xu, S. Qiao, Effective removal of selenate from aqueous solutions by the Friedel phase, *J. Hazard. Mater.* 176 (2010) 193-198.
- [30] R.L. Frost, S.J. Palmer, F. Theiss, Synthesis and Raman spectroscopic characterisation of hydrotalcites based on the formula  $\text{Ca}_6\text{Al}_2(\text{CO}_3)(\text{OH})_{16}\cdot 4\text{H}_2\text{O}$ , *J. Raman. Spectrosc.* 42 (2011) 1163-1167.
- [31] J.T. Klopogge, L. Hickey, R.L. Frost, FT-Raman and FT-IR spectroscopic study of synthetic Mg/Zn/Al-hydrotalcites, *J. Raman. Spectrosc.* 35 (2004) 967-974.
- [32] L. Châtelet, J. Bottero, J. Yvon, A. Bouchelaghem, Competition between monovalent and divalent anions for calcined and uncalcined hydrotalcite: anion exchange and adsorption sites, *Colloid. Surface. A.* 111 (1996) 167-175.

- [33] D.A. Long, Raman spectroscopy, McGraw-Hill International Book Company, New York, 1977.
- [34] J. Bensted, Uses of Raman spectroscopy in cement chemistry, *J. Am. Ceram. Soc.* 59 (1976) 140-143.
- [35] J. Ibáñez, L. Artús, R. Cuscó, Á. López, E. Menéndez, M.C. Andrade, Hydration and carbonation of monoclinic  $C_2S$  and  $C_3S$  studied by Raman spectroscopy, *J. Raman. Spectrosc.* 38 (2007) 61-67.
- [36] D. Bonen, T. Johnson, S. Sarkar, Characterization of principal clinker minerals by FT-Raman microspectroscopy, *Cem. Concr. Res.* 24 (1994) 959-965.
- [37] I. Richardson, J. Skibsted, L. Black, R.J. Kirkpatrick, Characterisation of cement hydrate phases by TEM, NMR and Raman spectroscopy, *Adv. Cem. Res.* 22 (2010) 233-248.
- [38] S. Martinez-Ramirez, M. Frías, C. Domingo, Micro-Raman spectroscopy in white portland cement hydration: long-term study at room temperature, *J. Raman. Spectrosc.* 37 (2006) 555-561.
- [39] L. Black, C. Breen, J. Yarwood, C.-S. Deng, J. Phipps, G. Maitland, Hydration of tricalcium aluminate ( $C_3A$ ) in the presence and absence of gypsum—studied by Raman spectroscopy and X-ray diffraction, *J. Mater. Chem.* 16 (2006) 1263-1272.
- [40] M. Tarrida, M. Madon, B. Le Rolland, P. Colombet, An in-situ Raman spectroscopy study of the hydration of tricalcium silicate, *Adv. Cem. Based. Mater.* 2 (1995) 15-20.
- [41] D. Torrén-Martín, L. Fernández-Carrasco, S. Martínez-Ramírez, Hydration of calcium aluminates and calcium sulfoaluminate studied by Raman spectroscopy, *Cem. Concr. Res.* 47 (2013) 43-50.
- [42] C.G. Kontoyannis, N.V. Vagenas, Calcium carbonate phase analysis using XRD and FT-Raman spectroscopy, *Analyst.* 125 (2000) 251-255.
- [43] G. Behrens, L.T. Kuhn, R. Ubig, A.H. Heuer, Raman spectra of vateritic calcium carbonate, *Spectrosc. Lett.* 28 (1995) 983-995.
- [44] S. Martinez-Ramirez, S. Sanchez-Cortes, J. Garcia-Ramos, C. Domingo, C. Fortes, M. Blanco-Varela, Micro-Raman spectroscopy applied to depth profiles of carbonates formed in lime mortar, *Cem. Concr. Res.* 33 (2003) 2063-2068.
- [45] M. Tlili, M.B. Amor, C. Gabrielli, S. Joiret, G. Maurin, P. Rousseau, Characterization of  $CaCO_3$  hydrates by micro-Raman spectroscopy, *J. Raman. Spectrosc.* 33 (2002) 10-16.
- [46] A. Brough, A. Atkinson, Micro-Raman spectroscopy of thaumasite, *Cem. Concr. Res.* 31 (2001) 421-424.
- [47] Y. Yue, J.J. Wang, P.M. Basheer, J.J. Boland, Y. Bai, Characterisation of carbonated Portland cement paste with optical fibre excitation Raman spectroscopy, *Constr. Build. Mater.* 135 (2017) 369-376.

- [48] Y. Yue, Y. Bai, P.M. Basheer, J.J. Boland, J.J. Wang, Monitoring the cementitious materials subjected to sulfate attack with optical fiber excitation Raman spectroscopy, *Opt. Eng.* 52 (2013) 104107-104107.
- [49] L. Black, C. Breen, J. Yarwood, K. Garbev, P. Stemmermann, B. Gasharova, Structural features of C–S–H (I) and its carbonation in air—a Raman spectroscopic study. Part II: carbonated phases, *J. Am. Ceram. Soc.* 90 (2007) 908-917.
- [50] E. Knittle, W. Phillips, Q. Williams, An infrared and Raman spectroscopic study of gypsum at high pressures, *Phys. Chem. Miner.* 28 (2001) 630-640.
- [51] L. Black, C. Breen, J. Yarwood, J. Phipps, G. Maitland, *In situ* Raman analysis of hydrating C<sub>3</sub>A and C<sub>4</sub>AF pastes in presence and absence of sulphate, *Adv. Appl. Ceram.* 105 (2006) 209-216.
- [52] A.C. Vieira, R.L. Moreira, A. Dias, Raman scattering and fourier transform infrared spectroscopy of Me<sub>6</sub>Al<sub>2</sub>(OH)<sub>16</sub>Cl<sub>2</sub>·4H<sub>2</sub>O (Me=Mg, Ni, Zn, Co, and Mn) and Ca<sub>2</sub>Al(OH)<sub>6</sub>Cl·2H<sub>2</sub>O hydrotalcites, *J. Phys. Chem. C*, 113 (2009) 13358-13368.
- [53] J.T. Kloprogge, D. Wharton, L. Hickey, R.L. Frost, Infrared and Raman study of interlayer anions CO<sub>3</sub><sup>2-</sup>, NO<sub>3</sub><sup>-</sup>, SO<sub>4</sub><sup>2-</sup> and ClO<sub>4</sub><sup>-</sup> in Mg/Al-hydrotalcite, *Am. Mineral.* 87 (2002) 623-629.
- [54] J. Ma, Z. Li, Y. Zhang, G.P. Demopoulos, Desilication of sodium aluminate solution by Friedel's salt (FS: 3CaO·Al<sub>2</sub>O<sub>3</sub>·CaCl<sub>2</sub>·10H<sub>2</sub>O), *Hydrometallurgy.* 99 (2009) 225-230.
- [55] P. Zhang, G. Qian, H. Cheng, J. Yang, H. Shi, R.L. Frost, Near-infrared and mid-infrared investigations of Na-dodecylbenzenesulfate intercalated into hydrocalumite chloride (CaAl-LDH-Cl), *Spectrochim. Acta. A.* 79 (2011) 548-553.
- [56] R.L. Frost, M.L. Weier, J.T. Kloprogge, Raman spectroscopy of some natural hydrotalcites with sulphate and carbonate in the interlayer, *J. Raman. Spectrosc.* 34 (2003) 760-768.
- [57] L. Black, Raman spectroscopy of cementitious materials in *Spectroscopic Properties of Inorganic and Organometallic Compounds*, volume 40, Royal Society of Chemistry, 2009.
- [58] E. Dubina, L. Korat, L. Black, J. Strupi-Suput, J. Plank, Influence of water vapour and carbon dioxide on free lime during storage at 80 °C, studied by Raman spectroscopy, *Spectrochim. Acta. A.* 111 (2013) 299-303.
- [59] A. Mesbah, C. Cau-dit-Coumes, F. Frizon, F. Leroux, J. Ravaux, G. Renaudin, A new investigation of the Cl<sup>-</sup>–CO<sub>3</sub><sup>2-</sup> substitution in AFm phases, *J. Am. Ceram. Soc.* 94 (2011) 1901-1910.
- [60] G. Renaudin, R. Segni, D. Mentel, J.-M. Nedelec, F. Leroux, C. Taviot-Gueho, A Raman study of the sulfated cement hydrates: ettringite and monosulfoaluminate, *J. Adv. Concr. Technol.* 5 (2007) 299-312.

- [61] J.T. Kloprogge, R.L. Frost, Fourier transform infrared and Raman spectroscopic study of the local structure of Mg-, Ni-, and Co-hydrotalcites, *J. Solid. State. Chem.* 146 (1999) 506-515.
- [62] A. Mesbah, J.P. Rapin, M. François, C. Cau-dit-Coumes, F. Frizon, F. Leroux, G. Renaudin, Crystal Structures and Phase Transition of Cementitious Bi-Anionic AFm-(Cl<sup>-</sup>, CO<sub>3</sub><sup>2-</sup>) Compounds, *J. Am. Ceram. Soc.* 94 (2011) 261-268.
- [63] G. Renaudin, F. Kubel, J.-P. Rivera, M. François, Structural phase transition and high temperature phase structure of Friedels salt, 3CaO·Al<sub>2</sub>O<sub>3</sub>·CaCl<sub>2</sub>·10H<sub>2</sub>O, *Cem. Concr. Res.* 29 (1999) 1937-1942.
- [64] A.G. Kalinichev, R.J. Kirkpatrick, R.T. Cygan, Molecular modeling of the structure and dynamics of the interlayer and surface species of mixed-metal layered hydroxides: chloride and water in hydrocalumite (Friedel's salt), *Am. Mineral.* 85 (2000) 1046-1052.
- [65] A.G. Kalinichev, R.J. Kirkpatrick, Molecular dynamics modeling of chloride binding to the surfaces of calcium hydroxide, hydrated calcium aluminate, and calcium silicate phases, *Chem. Mater.* 14 (2002) 3539-3549.
- [66] G. Renaudin, J.-P. Rapin, E. Elkaim, M. François, Polytypes and polymorphs in the related Friedel's salt [Ca<sub>2</sub>Al (OH)<sub>6</sub>]<sup>+</sup>[X·2H<sub>2</sub>O]<sup>-</sup> halide series, *Cem. Concr. Res.* 34 (2004) 1845-1852.
- [67] K. Garbev, P. Stemmermann, L. Black, C. Breen, J. Yarwood, B. Gasharova, Structural features of C-S-H (I) and its carbonation in air—a Raman spectroscopic study. Part I: fresh phases, *J. Am. Ceram. Soc.* 90 (2007) 900-907.